AIP | The Journal of Chemical Physics

Chemically driven fluid transport in long microchannels

Mingren Shen, Fangfu Ye, Rui Liu, Ke Chen, Mingcheng Yang, and Marisol Ripoll

Citation: The Journal of Chemical Physics **145**, 124119 (2016); doi: 10.1063/1.4963721
View online: http://dx.doi.org/10.1063/1.4963721
View Table of Contents: http://scitation.aip.org/content/aip/journal/jcp/145/12?ver=pdfcov
Published by the AIP Publishing

Chemically driven fluid transport in long microchannels

Mingren Shen,[1] Fangfu Ye,[1] Rui Liu,[1,a)] Ke Chen,[1,b)] Mingcheng Yang,[1,c)] and Marisol Ripoll[2]
[1]*Beijing National Laboratory for Condensed Matter Physics and Key Laboratory of Soft Matter Physics, Institute of Physics, Chinese Academy of Sciences, Beijing 100190, China*
[2]*Theoretical Soft-Matter and Biophysics, Institute of Complex Systems, Forschungszentrum Jülich, 52425 Jülich, Germany*

(Received 15 May 2016; accepted 15 September 2016; published online 30 September 2016)

Chemical gradients maintained along surfaces can drive fluid flows by diffusio-osmosis, which become significant at micro- and nano-scales. Here, by means of mesoscopic simulations, we show that a concentration drop across microchannels with periodically inhomogeneous boundary walls can laterally transport fluids over arbitrarily long distances along the microchannel. The driving field is the secondary local chemical gradient parallel to the channel induced by the periodic inhomogeneity of the channel wall. The flow velocity depends on the concentration drop across the channel and the structure and composition of the channel walls, but it is independent of the overall channel length. Our work thus presents new insight into the fluid transport in long microchannels commonly found in nature and is useful for designing novel micro- or nano-fluidic pumps. *Published by AIP Publishing.* [http://dx.doi.org/10.1063/1.4963721]

I. INTRODUCTION

Concentration gradients of solute molecules in solutions cannot only induce a diffusive mass flux but also transport surrounding materials by osmosis, electrochemical gradient, diffusiophoresis, or diffusio-osmosis.[1] Such gradient-driven transports on small scales are essential in biological systems.[2] Relevant examples include the passive osmosis of water molecules and the (secondary) active transport of ions through membrane. A recent work has even shown that the diffusio-osmotic force, arising from the interactions of nonuniform solute with channel boundaries, is critical for the activation of mechanosensitive channels.[3] On the other hand, chemical gradients have been exploited in synthetic microfluidic systems.[4–6] Particularly, the diffusio-osmosis was recently proposed to pump fluids,[7,8] manipulate mesoscale particles,[9,10] and to harvest chemical energy.[11] Further exploration and tailoring of the chemical gradient-driven transport will provide rich possibilities to manipulate fluids in lab-on-chip systems and new insights into the understanding of related transport phenomena in nature.

In most designs that utilize chemical gradients to transport fluids,[3,7–11] the chemical gradient is applied along the direction of the flow. This means that the flow is proportional to the concentration difference at the two ends of the channels, which severely hampers the transport of fluids in long micro-channels. Similar difficulties also occur for other types of pumping mechanisms, e.g., pressure gradient-driven micropumps where a huge pressure drop would be required. Thus, a chemically driven transport that is independent of the channel length will be particularly suitable to microfluidic systems with long microchannels, which also often exist in biology, geosciences (like submarine porous mineral precipitates), or petroleum engineering, where the chemical gradients are ubiquitous. Microchannels with an asymmetric sawtooth wall have been recently theoretically shown to be able to pump fluid by self-diffusiophoresis,[12] where the chemical inhomogeneity is created by wall-catalyzed chemical reactions. This theoretical work solves numerically the Stokes flow problem using a chemical gradient-induced slip flow boundary with a fixed constant solute flux and a constant diffusiophoretic mobility, which results in a weak overall fluid transport along the channel over long distances.

In this paper, we perform hybrid molecular simulations to study fluid transport by chemical gradients in micro-channels. We consider two different types of microchannel designs: a planar channel with periodically chemically heterogeneous boundaries and a chemically homogeneous channel with a ratchet-like geometry. In both cases, we show that a chemical gradient across the channel can drive a significant fluid flow along the channel by diffusio-osmosis. The driving force comes from the local concentration variations along the channel walls produced by the boundary asymmetries. The flow rate is independent of the channel length, which facilitates the transport of fluids in arbitrarily long microchannels. Experimentally, such a system corresponds to a narrow gap sandwiched by two reservoirs of different concentrations. The rest of the paper is organized as follows. In Sec. II, the microchannel model is described and the hybrid simulation method is introduced. Simulation results and discussions are presented in Secs. III and IV.

II. SIMULATION MODEL AND METHOD

To transport fluid in a microchannel by the diffusio-osmosis, a chemical gradient component parallel to the boundary, $\nabla c_{\parallel}$, is required, with the diffusio-osmotic flow

a)Electronic address: lr@iphy.ac.cn
b)Electronic address: kechen@iphy.ac.cn
c)Electronic address: mcyang@iphy.ac.cn

velocity $\mathbf{u}_d \sim \nabla c_{\|}$. Besides directly imposing a chemical difference at the two ends of a channel, one can rely on the inhomogeneities of the channel boundaries to create local concentration gradients along channel walls, starting from a concentration drop in between two channel walls. These local secondary gradients, together with the nearby boundary regions, can act as independent driving units that, when connected, will be able to pump flows over long distances. To produce a directed net transport, the driving elements must be non-symmetric either in their constituent materials or in their geometric structures.[13] The designs for these two types of driving units are separately described after the simulation method.

A. Simulation method

Hybrid molecular simulations in two dimensions are performed to investigate the capability of the pump devices of transporting a binary fluid. The fluid is described by multiparticle collision dynamics (MPC),[14–18] while the channel wall-fluid interactions are modeled by standard molecular dynamics (MD). In MPC, the fluid molecules are modeled as a large number of point particles of mass m, whose dynamics consists of alternating streaming and collision steps. In the streaming step, each fluid particle moves ballistically for a fixed time h. In the collision step, particles are sorted into square cells of size l_c and interact only with particles in the same cell. The binary fluid is accounted by two particle types, A and B. Both A and B-type particles take part in the MPC collision, where the particle species is not distinguished. We use the stochastic rotation collision rule with variable rotational angle α introduced by Ryder and Yeomans.[19,20] This collision rule locally conserves mass, linear momentum, angular momentum, and energy, and correctly captures hydrodynamic interactions, thermal fluctuations, mass diffusion, and dissipation. In our simulations, lengths are measured in units of l_c, energies in units of k_BT (k_B the Boltzmann constant), and masses in units of m, such that the flux through the channel is measured in units of $\sqrt{k_BT/ml_c^2}$. This corresponds to setting $m = 1$, $l_c = 1$, and $k_BT = 1$. We employ the standard MPC parameters, collision time $h = 0.1$, and mean number of fluid particles per cell $\rho = 10$. A kinetic theory calculation[21] allows us to obtain approached values for the fluid kinetic viscosity $\nu \simeq 0.76$, and the diffusion coefficient $D_s \simeq 0.06$. This produces a liquid-like dynamics with a Schmidt number $Sc \simeq 12$.

Walls are mostly simulated as an ensemble of spherical beads with strong tunable interactions with the surrounding fluid particles. The wall beads remain fixed during the simulation. The interactions between the fluid particles and the wall beads take place through Lennard-Jones (LJ) type potentials,

$$U_{kI}(r) = 4\epsilon\left[\left(\frac{\sigma}{r}\right)^{2n} - \left(\frac{\sigma}{r}\right)^{n}\right] + \epsilon', \mathbf{r} \le r_c, \qquad (1)$$

with ϵ being the potential intensity, n a positive integer number, σ the bead radius, r_c the cutoff, $\epsilon' = 0$ for attractive LJ potential, and $\epsilon' = \epsilon$ for repulsive one. Here, the subscript k and I refer to the kinds of the wall beads and the fluid molecules, respectively. For the sake of convenience, the notations $r(n, \epsilon)$ and $a(n, \epsilon)$ are used to, respectively, represent the repulsive and attractive LJ potentials. Between two consecutive MPC steps, 50 MD integration steps are performed with the velocity-Verlet algorithm, for the fluid particles near the wall beads.

The hybrid MPC-MD method employed here should be understood as a mesoscopic version of an all-atoms molecular dynamics simulation. Continuum equations can be recovered in certain limits, like large number of particles and collisions, and large length and time scales. This method is now well-established and its validity has been extensively verified.[17,18] Since this hybrid mesoscopic simulation can properly capture all the required essential physical features (i.e., hydrodynamics, mass diffusion, and diffusio-osmosis), the conclusions obtained from simulations are generally valid. The change in specific system parameters such as fluid density, viscosity, wall size, or wall-solvent interactions will only have a quantitative influence.

B. Planar multicomponent channel

We first propose a planar microchannel with multicomponent walls filled with a binary fluid mixture consisting of species A and B. The material heterogeneity of the boundary is required to produce a net directed flow. For simplicity, we simulate a two dimensional setup, but our results are straightforward to extrapolate to three dimensions as in previous related works.[20,22,23] Figure 1 illustrates the basic microchannel designs, where it can be seen that the walls are made by four different types of materials or structures with different functions.

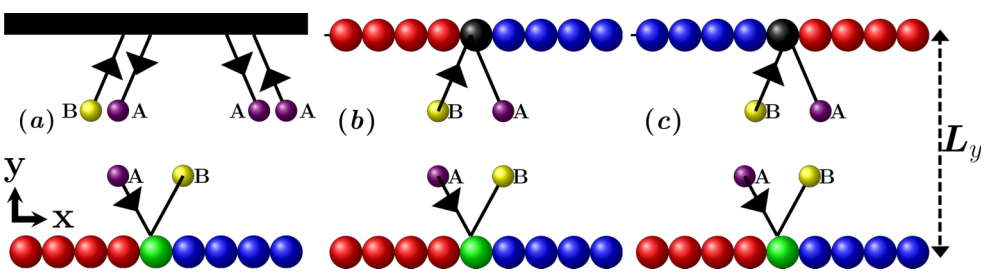

FIG. 1. Schematic diagram of planar channels with particle types specified in the text. In channel (a), the top boundary is a hard wall; in channels (b) and (c) the top wall consist of beads, with inverted bead sequence with respect to each other. To mimic the source and sink sites, chemical reactions are implemented at the corresponding places. Small beads inside the channel refer to the fluid particles.

Type 1 (depicted as green): Source of B-particles. Bead interactions with particles of type A and B are indistinguishable.
Type 2 (black): Sink of B-particles. Bead interactions with particles of type A and B are indistinguishable.
Type 3 (blue): Driving part of the channel wall, where the bead interactions with particle of type A is different from those with particle of type B.
Type 4 (red): Passive part of the channel wall, where the bead interactions with particles of type A and B are indistinguishable.

The combination of a source and a sink of B-particles (type 1 and 2 beads) establishes the chemical inhomogeneity. Experimentally, this may correspond to a channel sandwiched by two reservoirs characterized by different concentrations of B-particles.[24] At contact with the source and sink sites, solvent molecules of both types are exchanged with the external reservoirs by diffusion. Alternatively, the chemical inhomogeneity can be realized with a catalytic material at the source site (such as platinum), where a particular chemical reaction (such as $2H_2O_2 \rightarrow 2H_2O + O_2$) takes place,[25] and a reactant fuel reservoir in contact with the sink site. For simplicity, in the simulations we do not explicitly simulate the solution reservoirs that are connected to the channel through the source and sink sites, instead we mimic the source and sink by artificial chemical reactions. Similar schemes have been used in previous studies of chemically powered micromachines.[22,26–30] Specifically, the reaction $A \rightarrow B$ occurs upon a collision of A-particle with the source sites (green beads), and the inverse reaction occurs at the sink sites (black). The reaction takes place with an imposed probability P_r, by which the concentration of the reservoir is tuned. The source and sink regions can in principle be varied to larger or smaller sizes, but it should be large enough to be able to efficiently catalyze the chemical reactions. Since A and B particles generally interact with the beads through different potentials, conversion between species may lead to a local potential energy jump, as it happens in most real systems. This can heat the surrounding fluid and hence generate a local temperature gradient which can also eventually drive an additional thermo-osmotic flow. To focus here in the understanding of a pure diffusio-osmosis effect, we consider a reaction rule that avoids the local potential jump. This is achieved by imposing that the particle conversion only occurs for the reactant particles that have collided with the catalytic beads and just come out from the catalytic site with their current solvent-bead distances beyond the maximum interaction range of U_{kA} and U_{kB}.[22] This criterion assures that the reaction takes place locally around the catalytic site without potential change. Although the boundary catalytic operation in the simulations does not input external energy into the system, it continuously decreases the system entropy by changing the particle species such that it maintains the system out-of-equilibrium. Such Maxwell-demon-type boundary conditions do not affect physical processes within the system and have been quite widely used to generate non-equilibrium states in similar simulation setups.[26,31,32] When the system is connected to real reservoirs, it will be driven out of equilibrium by the combining energy and entropy input related to particle exchange.

Beads of type 3 and 4 are made of two different materials, which are used to break down space symmetry to generate a directed fluid motion. The necessary material heterogeneity of the boundary is incorporated in the simulations through different interaction potentials between fluid particles B and the beads on the wall. We perform a simple choice in which $U_{1A} = U_{1B} = U_{2A} = U_{2B} = U_{3A} = U_{4A} = U_{4B} = r(24, 1)$ are always fixed and U_{3B} is varied, with the bead radius $\sigma = 2.0$. As a consequence, the concentration inhomogeneity can only be felt by beads of type 3, and hence beads of type 3 and 4 correspond to the driving and passive parts of the channel wall, respectively. The specific form of the interaction potentials is not critically important, and a directed fluid flow will be produced when the channel boundary is heterogeneous.

In Fig. 1(a) the black surface refers to a hard wall simulated via bounce-back interaction reproducing sticky boundary condition. The source and sink sites on the boundaries create a concentration gradient of molecules B across the channel, as well as a lateral secondary gradient along the multicomponent wall (Fig. 3(a)) due to nonuniform distribution of the source sites on the bottom boundary. Two variants of the basic design are illustrated in Figs. 1(b) and 1(c), which replace the top hard wall by multi-bead wall with different bead arrangements.

Finally, in order to maintain a stationary flow, periodic boundary conditions are used in the non-confining channel direction (x-axis). These boundaries have two experimental counterparts: (1) a cycling channel loop (similar to blood circulation system), where the fluid is continuously transported through a closed channel; (2) a microchannel connected to two very large reservoirs at the two ends of the channel, where the hydrostatic pressure in the reservoirs varies only slightly due to their large cross sections.

C. Asymmetric ratchet channel

Another way of breaking down the spatial symmetry to induce a directed flow is purely geometrical. The design for a ratchet-like channel is shown in Fig. 2. One wall is

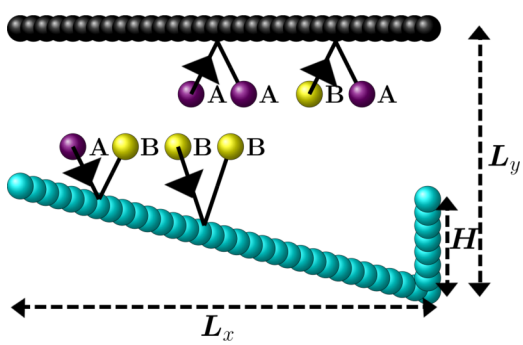

FIG. 2. Schematic diagram of ratchet channel. The whole sawtooth wall corresponds to the source of species B and the flat wall to the sink. L_y, L_x, and H denote the dimensions of a driving unit, which are, respectively, the channel width, and the sawtooth length and height.

sawtooth-shaped, and the other wall is flat. The constituent beads of the two walls have different interactions with the solvent particles. The whole flat wall is a B-sink where bead interactions with particles A and B are indistinguishable, similar to type 2 particles represented in black. Meanwhile, the sawtooth wall acts as both the B-source and the driving part, which is a combination of bead types 1 and 3 and is drawn in cyan in Fig. 2. The source and sink are also modeled by the catalytic chemical reaction. The effective contact area of the binary fluid with the B-source surface is larger near the cleft of the sawtooth than near the summit, which translates into a secondary chemical gradient parallel to the sawtooth edges. This secondary chemical gradient induces a diffusio-osmotic flow.

For the ratchet channel, we use again LJ-type potentials to describe the interactions between the fluid and the wall beads. Throughout the simulations, the radius of the wall beads is set to $\sigma = 1.5$, for the beads of the sawtooth wall $U_{3A} = r(3,2)$ and $U_{3B} = r(3,0.5)$ are chosen, and for the flat wall beads $U_{4A} = U_{4B} = r(24,1)$ are considered. Similar geometric asymmetry has been successfully applied in the design of self-phoretic microgears[20,22] and recently also to thermoosmotic micromachines.[23]

III. RESULTS AND DISCUSSION

A. Planar multicomponent channel

The simulations are initialized with all the fluid particles being species A. Stationary concentration distributions can be established quickly through the reactions on the channel walls. Figure 3(a) displays the relative concentration distribution of species B in a channel with four repeated units as those in Fig. 1(a). The four concentration centers correspond to four source sites (reaction regions) on the channel. The concentration of B molecules decreases from the source centers, creating chemical gradients across, as well as along, the channel. The lateral gradient is roughly symmetric with respect to the source sites, thus it does not provide directional bias to induce a net flow in the channel. The directed flow arises from the concentration gradient and the asymmetry of the solvent-wall interactions with type 3 (blue, and driving part of the wall) and type 4 (red, and passive part of the wall) wall beads. Our simulations used $U_{3B} = a(12,1)$ and $r(24,1)$ for all other interactions so that the 4-type beads cannot feel the chemical gradients, in contrast to the 3-type beads. This means that B particles exert a net attractive force on the 3-type beads parallel to the wall along its gradient (i.e., toward the source), while A particles exert a net repulsive force on the 3-type beads parallel to the wall against its gradient (i.e., also toward the source). Thus, the diffusiophoretic force exerted on the wall by both A and B fluid particles is directed toward the source.[29] The reaction of the diffusiophoretic force is the diffusio-osmotic force on the fluid, generating a diffusio-osmotic flow away from the source within the driving region, which in the case of Fig. 3(b) corresponds to a flow pointing to the right.

Note that if the top B-sink hard wall is replaced by a wall consisting of type 2 beads, the resulting flow field will be very similar, since these only passively contribute to the friction force. Comparing with the hard sticky wall, the wall composed of type 2 beads results in a partially slip boundary condition owing to the smooth potential interactions, and hence in a smaller friction. In this way, the flow in the case of the hard wall is slightly weaker than that in the case of type-2 bead wall. We here use the hard wall, to minimize the computational cost.

Since the diffusio-osmosis is a surface-driven effect, the flow patterns are sensitive to the surface properties of the channel wall. Thus, by tuning the wall properties we can easily manipulate the flow field. Figure 4 shows different flow fields obtained under different surface conditions. The flow field in Fig. 3(b) can be reversed by switching the interaction potential between molecule B and type-3 spheres (blue) from attractive to repulsive, as shown in Fig. 4(a). When the top wall of the channel is replaced by a mirror image of the bottom wall (Fig. 1(b)), with inverse reaction at the sink regions, the transport flow vanishes. A vortex is generated close to each driving unit, as shown in Fig. 4(b). The vortex structure originates from the opposite diffusio-osmosis induced by the two opposite walls. A different configuration shown in Fig. 1(c) reverses the location of the driving elements (blue beads) on the two opposite walls, such that they cooperate to drive the fluid in the same direction which clearly enhances

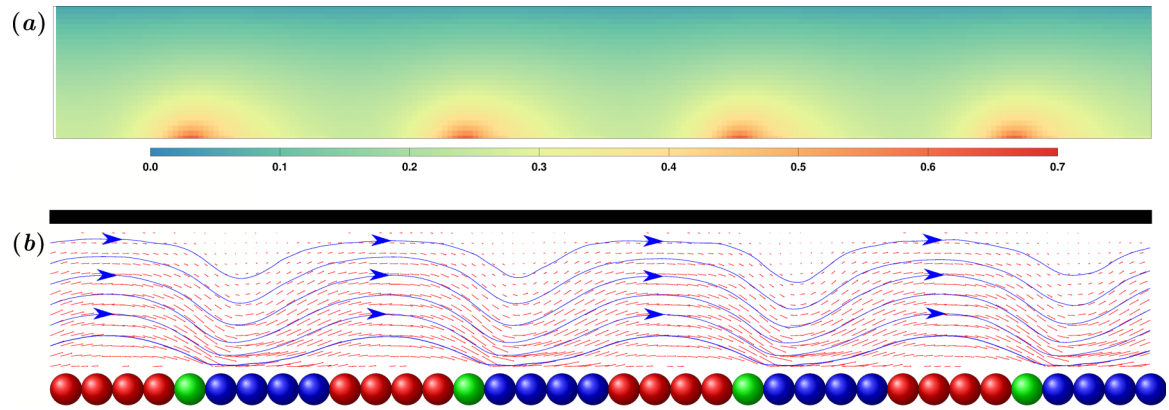

FIG. 3. Typical steady-state concentration distribution of species B (a) and flow field (b) in the planar channel of Fig. 1(a). B-particle concentration in (a) is measured in molar fraction, ρ_B/ρ; and the blue lines in (b) refer to the streamline. Here, $U_{3B} = a(12,1)$ and $L_y = 16$ are used, and the transition probabilities of particles in the source and sink regions are set as $Pr = 0.55$ and 0.1, respectively.

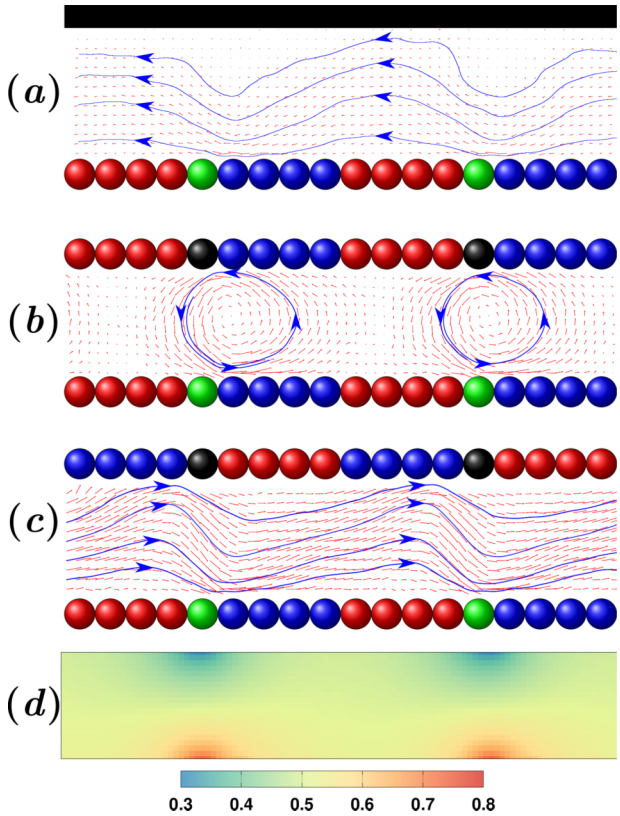

FIG. 4. Flow field in the planar channel of different boundaries. (a) The configuration is the same as that of Fig. 3 but uses $U_{3B} = r(3,1)$ instead of $a(12,1)$. (b) The bottom and top walls are symmetric with respect to the central axis of the channel, as depicted in Fig. 1(b). Here, $U_{3B} = a(12,1)$ is used. Systems (c) and (b) only differ in the position of 3 and 4-type beads of the top walls. (d) Steady-state concentration distribution of species B in the systems of (b).

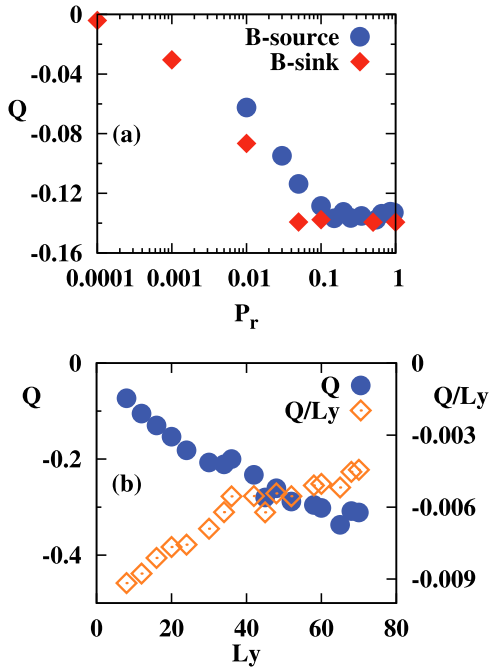

FIG. 5. Total fluid flux as a function of (a) the transition probability and (b) the channel width. Other system parameters are the same as those of Fig 4(a). The positive direction of the flow points to the right along the channel. In panel (a) symbols refer to changing Pr of the B-source or the B-sink walls keeping the other one fixed (0.1 for B-sink or 0.55 for B-source, respectively). Here, $L_y = 16$ is used. In panel (b) the circles denote the total flux, and the diamonds the mean flux density, Q/L_y. Pr at the B-source and sink sites is set as $Pr = 0.85$ and 0.1, respectively.

the overall fluid flux. Note that the steady-state concentration distribution of particles B is determined by the location of the source and the sink sites and it is similar for the configurations in Figs. 1(b) and 1(c), as shown in Fig. 4(d). Similarly, the concentration distribution of particles B corresponding to Fig. 3(a) is similar to that of Fig. 4(a).

Besides the surface properties of the channel walls, other parameters like the channel width L_y and the concentration gradient across the channel (determined by the reaction probability Pr) have important influence in the magnitude of the net flux. Figure 5 plots the total flux, Q, across the section of the channel,

$$Q = \int_0^{L_y} \rho u dy, \tag{2}$$

as a function of Pr and L_y, with u being the local flow velocity in the x-direction. The net flux rapidly increases with the reaction probability and saturates around 10% (Fig. 5(a)). Given the transition probability for one wall, higher reaction rate at the other wall results in higher concentration of the product molecules at the reaction sites, thus higher average gradient across and along the channel, shown in Fig. 3(a). However, when the reaction rate continues to increase, the product molecule cannot diffuse out of the reaction sites fast enough, and the reactants cannot promptly diffuse to the reaction sites. This diffusion-limited reaction results in a maximum concentration gradient across the channel, which determines the saturation of the flux.

When keeping other parameters fixed, the total flux increases with L_y due to larger cross section areas, while the mean flux density decreases, as shown in Fig. 5(b). This reflects the fact that the flux is driven locally by the wall surface instead of the bulk of the fluid. To explicitly quantify this, the local flow velocity across the channel of Fig. 4(a) as a function of the distance to the B-source wall is measured in Fig. 6(a). The flow velocity decreases linearly from the bottom to top wall, which clearly indicates that the flow pattern observed in our simulations can be attributed to the driving from the bottom boundary. Figure 6(b) plots the flow velocity in a layer neighbouring the B-source wall in the driving regions. The flow velocity is calculated for various values of Pr of the B-source bead, such that the dependence on the local lateral chemical gradient $\nabla c_{\|}$ is obtained. The linear relation between the boundary flow and local gradients confirms that the driving mechanism is the diffusio-osmosis due to the chemical gradients along the boundary. With the typically measured flow velocities, the Reynolds numbers can be calculated in the range $10^{-1} - 10^{-2}$ such that the flow field can be well described by the Stokes equation, and the Peclet number is around 0.2, implying that the advective effects are weak relative to the diffusion of solvent molecule.

It would be instructive to discuss the non-equilibrium thermodynamic basis of the present microdevice. In the simulations, the system is maintained out-of-equilibrium using the catalytic chemical reaction on the boundary walls. Given

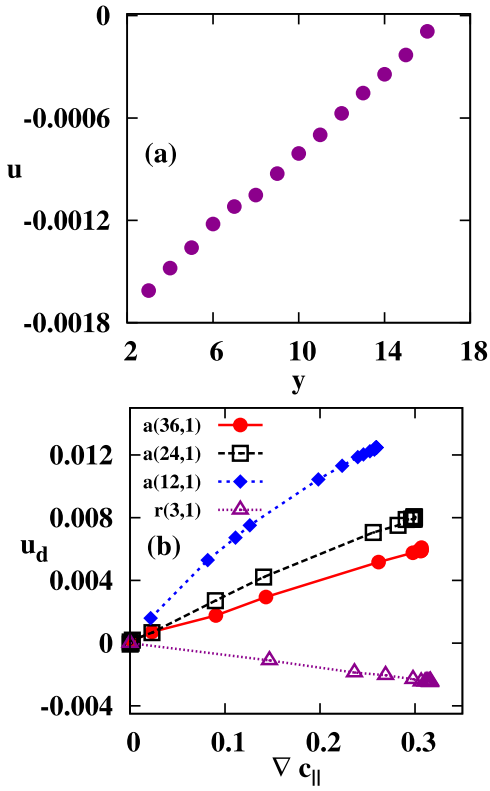

FIG. 6. (a) Local flow velocity across the channel in Fig. 4(a) with $U_{3B} = r(3,1)$ and $\nabla c_{\|} \simeq 0.32$ (Pr = 0.55 and 0.1 separately at B-source and sink) as a function of the distance to the B-source wall. (b) Diffusio-osmotic flow velocity as a function of the tangential concentration gradient of species B within the driving region, with $L_y = 16$. Symbols correspond to different choices of U_{3B}.

in the presence of concentration difference across the channel, our simulation results satisfy the first law of thermodynamics, since the total energy of system (including the internal energy and the kinetic energy of macroscopic flow) is conserved. The kinetic energy of macroscopic flow is extracted from the system internal energy through the diffusio-osmotic effect; meanwhile the macroscopic kinetic energy is dissipated into the internal energy by friction. The system reaches the steady state when these two processes balance each other. On the other hand, the second law of thermodynamics prohibits extraction of directed transport (useful work) from a single equilibrium thermal bath. However, the proposed device does not violate the second law of thermodynamics because it is in a non-equilibrium state, which renders inoperative those limiting thermal equilibrium restrictions. Another important example of such non-equilibrium micromachines is the Brownian motors.[33,34]

We finally roughly evaluate the transport capacity of a diffusio-osmotic channel pump of Fig. 1 in real applications. Diffusio-osmotic velocity experimentally achievable is typically in the range of $1 - 10$ μm s^{-1}.[1,10] In our design, the flows are driven by the secondary lateral gradient on the boundary, which therefore would be slightly weaker than the primary gradient across the channel, as shown Fig. 3(a). The secondary gradient can be largely enhanced by reducing the channel width L_y. Thus, it is reasonable to expect that the diffusio-osmotic flow in a real heterogeneous channel can reach the magnitude similar to those reported in the previous studies. Moreover, it has been demonstrated that the diffusio-osmotic flow at a (partial) slip surface such as the superhydrophobic surface may be amplified by more than 3 orders of magnitude.[7,35] Thus, in a heterogeneous microchannel with superhydrophobic surfaces, the induced secondary chemical gradient could drive a significant diffusio-osmotic transport.

B. Asymmetric ratchet channel

Figure 7(a) plots the spatial distribution of the concentration of molecule B in the steady state. The highest concentrations of B molecules are found at the clefts of the sawtooth wall (lowest for A molecules). This is caused by a pure geometrical effect, as explained in Sec. II C. The tangential gradients along both the long and short edges point toward the cleft. This generates two competing diffusio-osmotic flows along both edges, leading to a vortex near each cleft, together with a net lateral flow along the channel, as shown in Fig. 7(b). In this case, the interactions between the sawtooth wall and the fluid molecules are chosen to be $U_{3A} = r(3,2)$ and $U_{3B} = r(3,0.5)$. The stronger U_{3A} pushes the fluid toward the summit region along both the short and long edges, where A molecules are more concentrated. Thus, the net flow in the channel is directed to the left, with counter-clockwise vortices near the short edges.

The flow field can be reversed when the reactions at the flat and the ratcheted walls or the potentials U_{3A} and U_{3B} are switched. Figure 8 shows a reversed flow field in a ratchet channel, with the flat wall being the source of B-type fluid particles. On the other hand, if the sawtooth wall is symmetric as in Fig. 9, the non-vanishing diffusio-osmotic

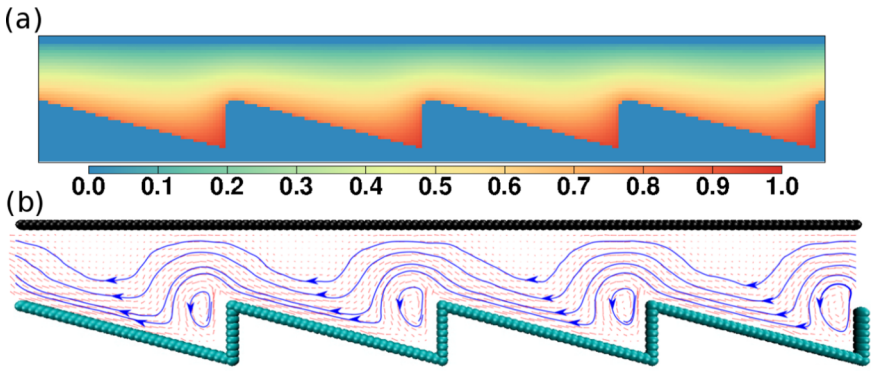

FIG. 7. (a) The steady-state relative concentration distribution of species B, ρ_B/ρ, and (b) the diffusio-osmosis induced flow field in the ratchet channel, with $L_x = 31$, $L_y = 20$, and $H = 8$. Here, the transition $A \to B$ uniformly occurs at the bottom wall with $Pr = 0.55$, and $B \to A$ at the top wall with $Pr = 0.1$.

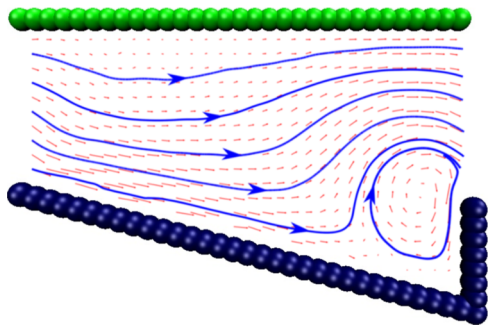

FIG. 8. Flow field induced by a chemical gradient in a ratchet channel, with the reaction $B \rightarrow A$ at the bottom wall and $A \rightarrow B$ at the top wall. Here, the bottom sawtooth wall acts as both B-sink and the driving part, and is drawn in dark blue. Other system parameters are the same as those of the ratchet channel in Fig. 7.

flows along each of the two tooth edges cause counter-rotating vortexes. These are though perfectly symmetric such that the net flow through the channel vanishes in this geometry. As the asymmetry of the sawtooth wall increases, a smooth asymmetric distortion of the two counter-rotating vortexes and a traversing flow through the channel is expected. Determined by the boundary geometry, each vortex will change its velocity, size, shape, and stagnation point position. In our geometry, a change in the length of the ratchet edges modifies the related gradients, such that the vortex becomes slower/faster when the corresponding sawtooth wall is enlarged/shortened. Given the large asymmetry of the channels employed in this work, the transversal flow lines dominate, and it is not possible to clearly distinguish (see Figs. 7 and 8) if there is a weak remaining vortex of the long edge.

For the basic design of ratchet channels in Fig. 2, we examine the various parameters that are expected to influence the total transport capacity of the channel. Similar to planar channels, the total flux through the ratchet channel increases with the reaction probability Pr and saturate at $Pr \sim 10\%$ as shown in Fig. 10(a). The total flux also increases with the channel width, while the flux density decreases, as plotted in Fig. 10(b). A unique parameter for ratchet channels is the wall height H that tunes the geometric asymmetry of the channel when L_x and L_y are fixed. For $H = 0$, the channel becomes a planar channel with homogeneous chemical properties, thus cannot induce a fluid flow. As H increases, both the geometric bias and impedance to the flow increase. Thus, there exists an optimal H that maximizes the net flux through the channel. Figure 10(c) shows that the net flux increases with the wall height and then decreases when H is further increased beyond $H \simeq 8$.

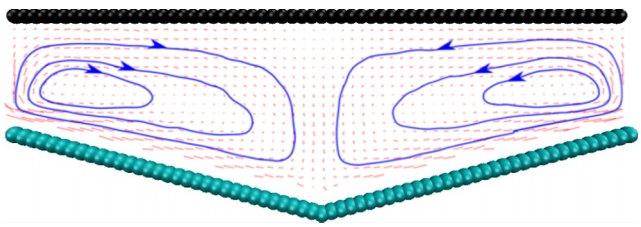

FIG. 9. Flow field in a symmetric ratchet channel. Here, the bead-fluid interactions and the transition probabilities are the same as those in Fig. 7.

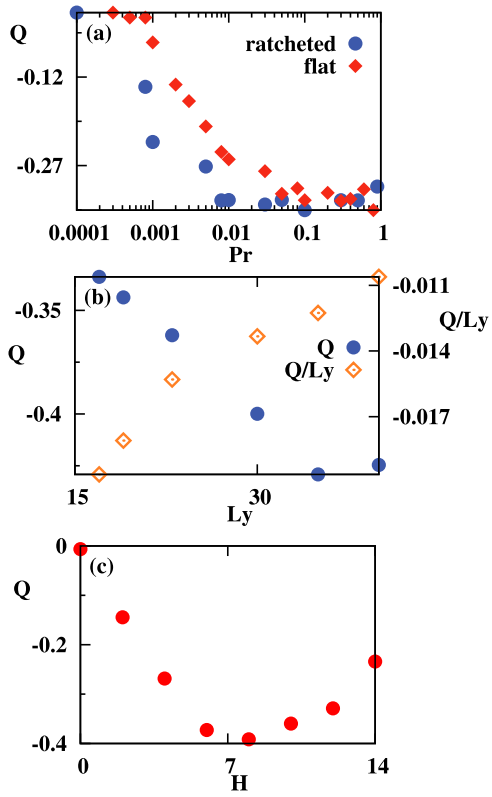

FIG. 10. The total flux through a ratchet channel as a function of (a) the transition probability, (b) the channel width, and (c) the wall height. The positive direction of the flow points to the right along the channel. In the case of (a), $L_x = 31$, $L_y = 20$, and $H = 8$ are set, and the circles and squares separately refer to the independent change of Pr at the ratcheted or flat wall, keeping the other fixed (0.1 for the flat wall or 0.55 for the ratcheted wall). In the case of (b), $L_x = 31$ and $H = 8$ are fixed, and the diamonds denote the mean flux density. In the case of (c), $L_x = 31$ and $L_y = 20$ are fixed. Both (b) and (c) take $Pr = 0.55$ for the ratcheted wall, while $Pr = 0.1$ and 0.5 are, respectively, considered for the flat wall.

In a very recent theoretical work,[12] a similar ratchet channel has been proposed to pump fluids by auto-diffusiophoresis. In that work, the full Stokes flow problem is numerically solved and the obtained flow patterns show noticeably different from the present simulations, as can be seen in the locations of the traversing streamlines. In the numerical approach, the traversing streamlines are located very close to the short edges, while with our simulations these are closer to the long edges, giving rise to significantly larger fluid fluxes. The possible origin of the differences is the boundary conditions employed in both cases. In the numerical calculation, a fixed constant solute-flux boundary and a constant diffusiophoretic mobility along the sawtooth edges are imposed. Thus, this approach did not account for any possible concentration-dependence of the solute flux and the diffusiophoretic mobility. In the simulations, we fix the reaction probability instead of the solute flux, and the diffusiophoretic mobility results from the direct interactions of the fluid particles with wall, such that the solute flux and phoretic mobility along the edges are not necessary constant and can depend on the solute concentration. Moreover, the present simulations properly take into account thermal fluctuations, which are known to play an important role on mesoscales.

IV. CONCLUSIONS

We have performed hybrid dynamic simulations to study fluid transport in microscale channels under a concentration change across the channel. We show that in the presence of periodic surface heterogeneities or geometric asymmetry of the channel boundaries, a lateral flow can be obtained. The flow is driven by diffusio-osmosis resulting from the local secondary gradients parallel to the channel boundary. These can be induced by the boundary inhomogeneities combined with the primary gradient across the channel. Because each periodic structure of the microchannel is an independent driving unit, the net flow does not depend on the channel length. Moreover, the magnitude and structure of the resulting flow field is sensitive to the diffusio-osmotic properties of the channel wall, which allows us to flexibly control micro-flow field. Our results could be employed to better understand fluid transport in long capillaries frequently found in nature. Moreover, the obtained perspective can provide novel strategies to pump fluids in long synthetic micro- or nano-channels.

ACKNOWLEDGMENTS

We thank Roland G. Winkler for useful discussions. We acknowledge the financial support of the NSFC (Grant Nos. 11674365, 11404379, 11474327, and 11404378). This work was also supported by the MOST 973 Program (Grant No. 2015CB856800). K.C. acknowledges the support from "The Recruitment Program of Global Youth Experts" of China. M.R. gratefully acknowledges financial support by the Deutsche Forschungsgemeinschaft via SPP 1726 Microswimmers.

[1]J. L. Anderson, Annu. Rev. Fluid Mech. **21**, 61 (1989).
[2]B. Alberts, A. Johnson, J. Lewis, M. Raff, K. Roberts, and P. Walter, *Molecular Biology of the Cell* (Garland Science, New York, 2002).
[3]D. J. Bonthuis and R. Golestanian, Phys. Rev. Lett. **113**, 148101 (2014).
[4]T. M. Squires and S. R. Quake, Rev. Mod. Phys. **77**, 977 (2005).
[5]B. Abécassis, C. Cottin-Bizonne, C. Ybert, A. Ajdari, and L. Bocquet, Nat. Mater. **7**, 785 (2008).
[6]J. Palacci, B. Abécassis, C. Cottin-Bizonne, C. Ybert, and L. Bocquet, Phys. Rev. Lett. **104**, 138302 (2010).
[7]D. M. Huang, C. Cottin-Bizonne, C. Ybert, and L. Bocquet, Phys. Rev. Lett. **101**, 064503 (2008).
[8]J. J. McDermott, A. Kar, M. Daher, S. Klara, G. Wang, A. Sen, and D. Velegol, Langmuir **28**, 15491 (2012).
[9]A. Reinmüller, E. Oğuz, R. Messina, H. Löwen, H. Schöpe, and T. Palberg, J. Chem. Phys. **136**, 164505 (2012).
[10]V. Yadav, H. Zhang, R. Pavlick, and A. Sen, J. Am. Chem. Soc. **134**, 15688 (2012).
[11]A. Siria, P. Poncharal, A.-L. Biance, R. Fulcrand, X. Blase, S. T. Purcell, and L. Bocquet, Nature **494**, 455 (2013).
[12]S. Michelin, T. D. Montenegro-Johnson, G. De Canio, N. Lobato-Dauzier, and E. Lauga, Soft Matter **11**, 5804 (2015).
[13]R. Feynman, *The Feynman Lectures on Physics* (Addison-Wesley, Reading, 1963).
[14]A. Malevanets and R. Kapral, J. Chem. Phys. **110**, 8605 (1999).
[15]M. Ripoll, K. Mussawisade, R. G. Winkler, and G. Gompper, Phys. Rev. E **72**, 016701 (2005).
[16]J. T. Padding and A. A. Louis, Phys. Rev. E **93**, 031402 (2006).
[17]R. Kapral, Adv. Chem. Phys. **140**, 89 (2008).
[18]G. Gompper, T. Ihle, D. M. Kroll, and R. G. Winkler, Adv. Polym. Sci. **221**, 1 (2009).
[19]J. F. Ryder, "Mesoscopic simulations of complex fluids," Ph.D. thesis, University of Oxford, 2005.
[20]M. Yang and M. Ripoll, Soft Matter **10**, 1006 (2014).
[21]E. Tüzel, T. Ihle, and D. M. Kroll, Phys. Rev. E **74**, 056702 (2006).
[22]M. Yang, M. Ripoll, and K. Chen, J. Chem. Phys. **142**, 054902 (2015).
[23]M. Yang and M. Ripoll, Soft Matter (2016).
[24]J. Palacci, C. Cottin-Bizonne, C. Ybert, and L. Bocquet, Phys. Rev. Lett. **105**, 088304 (2010).
[25]J. R. Howse, R. A. L. Jones, A. J. Ryan, T. Gough, R. Vafabakhsh, and R. Golestanian, Phys. Rev. Lett. **99**, 048102 (2007).
[26]G. Rückner and R. Kapral, Phys. Rev. Lett. **98**, 150603 (2007).
[27]Y. G. Tao and R. Kapral, J. Chem. Phys. **128**, 164518 (2008).
[28]Y. G. Tao and R. Kapral, Soft Matter **6**, 756 (2010).
[29]M. Yang, A. Wysocki, and M. Ripoll, Soft Matter **10**, 6208 (2014).
[30]M. Yang, R. Liu, M. Ripoll, and K. Chen, Lab Chip **15**, 3912 (2015).
[31]F. Müller-Plathe, J. Chem. Phys. **106**, 6082 (1997).
[32]F. Müller-Plathe, Phys. Rev. E **59**, 4894 (1999).
[33]P. Reimann, Phys. Rep. **361**, 57 (2002).
[34]P. Hänggi and F. Marchesoni, Rev. Mod. Phys. **81**, 387 (2009).
[35]A. Ajdari and L. Bocquet, Phys. Rev. Lett. **96**, 186102 (2006).